Available online at www.sciencedirect.com
ScienceDirect
C. R. Chimie 12 (2009) 731–739
COMPTES RENDUS CHIMIE

Full paper/Mémoire

Preparation and characterisation of metal oxides supported on SBA-15 as methane combustion catalysts

Guillaume Laugel [a,*], Jaouad Arichi [a], Pierre Bernhardt [a], Michel Molière [b], Alain Kiennemann [a], François Garin [a], Benoît Louis [a]

[a] *Laboratoire des matériaux, surfaces et procédés pour la catalyse, LMSPC – UMR 7515 du CNRS – ECPM – ULP, 25, rue Becquerel, 67087 Strasbourg, France*
[b] *GE Energy Products – Europe (GEEPE), 20, avenue du Maréchal Juin, 9007 Belfort cedex, France*

Received 5 May 2008; accepted after revision 17 September 2008
Available online 14 March 2009

Abstract

A high dispersion of Co_3O_4 and Mn_3O_4 nanoparticles on SBA-15 mesoporous silica was carried out thanks to a two-solvent impregnation method. This kind of preparation allows a proper control of both the metal oxides loading (7 or 30 wt.%) and the particle sizes (10–12 nm). A complete set of physico-chemical characterisations of Co_3O_4 and Mn_3O_4 supported oxides on SBA-15 was realized using several techniques such as XRD, BET, TEM and XPS, to correlate the structures of the materials with their catalytic activities.

Co_3O_4/SBA-15 and Mn_3O_4/SBA-15, 7% in weight, exhibit a high catalytic performance in the combustion of methane under Lower Explosive Limit (LEL) conditions, comparable to the well-known $LaBO_3$ (B = Co or Mn) perovskite-type. The efficiency of the catalysts can be explained by the organised porous meso-structure of the SBA-15. Indeed, the mesoporous support creates a confinement medium which permits a high dispersion of metal oxide nanoparticles. The Co_3O_4 and Mn_3O_4 nanoparticles supported on SBA-15 become therefore novel efficient combustion catalysts at low metal oxides' loading. ***To cite this article: G. Laugel et al., C. R. Chimie 12 (2009).***

Résumé

Des nanoparticules de Co_3O_4 et de Mn_3O_4 ont été dispersées de manière homogène sur de la silice mésoporeuse SBA-15 à l'aide de la méthode d'imprégnation appelée ≪deux-solvants≫. Ce type de préparation permet un contrôle efficace à la fois de la quantité d'oxydes métalliques déposés (7 ou 30 wt.%) et de la taille des particules (10–12 nm). Une caractérisation poussée des oxydes Co_3O_4 et Mn_3O_4 supportés sur la SBA-15 a été entreprise en utilisant différentes techniques telles que DRX, BET, MET et XPS afin de corréler leurs structures avec leurs activités catalytiques.

Les matériaux Co_3O_4/SBA-15 et Mn_3O_4/SBA-15 à 7% en masse, présentent une très bonne activité catalytique dans la combustion du méthane, comparable à celle des pérovskites de type $LaBO_3$ (B = Co ou Mn), dans les conditions de la Limite Inférieure d'Explosivité (LIE) du gaz. L'efficacité de ces catalyseurs peut être expliquée par la structure organisée en mésopores de

* Corresponding author.
E-mail address: glaugel@chimie.u-strasbg.fr (G. Laugel).

1631-0748/$ - see front matter © 2009 Académie des sciences. Published by Elsevier Masson SAS. All rights reserved.
doi:10.1016/j.crci.2008.09.031

la SBA-15. En effet, le support mésoporeux crée un milieu confiné qui permet une grande dispersion des nanoparticules d'oxydes métalliques. Les nanoparticules de Co_3O_4 et de Mn_3O_4 supportées sur la SBA-15 deviennent ainsi des catalyseurs de choix pour la combustion catalytique, à faible teneur en oxydes métalliques. ***Pour citer cet article : G. Laugel et al., C. R. Chimie 12 (2009).***

Keywords: Metal oxides; SBA-15; Mesopores; Catalytic combustion; Methane

Mots-clés : oxydes métalliques ; SBA-15 ; mésopores ; combustion catalytique ; méthane

1. Introduction

In gas turbine units, recent safety recommendations require a limited level of explosive exhaust gases corresponding to 5% LEL (Lower Explosive Limit) for methane [1–3]. A rapid detection and signal warning can be obtained by the use of a catalytic combustion sensor. The principle of this kind of detector is based on the measurement of the gas concentration as a function of the temperature increase produced by the heat of reaction at the catalyst surface [4–6]. It becomes thus necessary to develop efficient catalysts for complete methane oxidation at relatively low concentration and temperature (below 600 °C). The catalytic surface is generally composed of noble metal particles (Pt or Pd) on support like γ-Al_2O_3 [1,7,8]. However, metal oxides M_yO_x (M = Co or Mn) and mixed metal oxides, *i.e.* perovskites [9–11], pyrochlores [12], offer an interesting alternative to noble metals with both an improvement in thermal stability and a lower cost.

An inconvenience with the metal oxides is their poor specific surface area (SSA) which seriously hinders their efficiency as catalysts. To overcome this drawback, solutions are either to impregnate metal oxide nanoparticles on a support, or to disperse them within a porous host having a high specific surface area (SSA). Mesoporous silica SBA-15 is a promising candidate as catalyst support [13–17], since this material presents a high SSA (600–1000 m^2/g) and consists in a hexagonal array of uniform tubular-channels with tunable pore diameter in the range of 5–30 nm. Furthermore, thanks to its thicker walls (3–6 nm), SBA-15 exhibits a higher thermal and hydrothermal stability when compared to MCM-type mesoporous silica. SBA-15 sample is generally synthesized according to the procedure described by Zhao et al. [18] using Pluronic tri-block copolymer (EO_{20}–PO_{70}–EO_{20}, P123, BASF) as structure-directing agent and tetraethyl orthosilicate (TEOS) as silica source under strongly acidic conditions.

Conventional procedures to coat oxides remain impregnation and ion exchange techniques. Recently a novel method, based on the different hydrophilicity of two solvents, has attracted a considerable interest because of the high dispersion of metal oxide nanoparticles within silica mesopores, being used as confinement nanoreactors [19,20]. This method consists of firstly in suspending the silica host in *n*-hexane before contacting them with an aqueous metal oxide solution of volume set equal to the silica porous volume. Secondly, a calcination under air flow was used to induce the precursor transformation into its oxides. It is noteworthy that the metal oxide loading should remain low enough to insure a proper pore filling. Indeed, after metal oxide crystallization, the pores and the channel structure of the host materials need to be accessible for reactants to achieve a high catalytic activity.

The present study deals with the synthesis and characterisation of Co_3O_4 and Mn_3O_4 nanoparticles selectively grown inside a mesoporous SBA-15 silica support. The obtained materials were characterised by XRD at low- and wide-angle to determine the crystalline phases. The effect of the metal oxide impregnation on the surface area and pore size of SBA-15 was examined by nitrogen adsorption–desorption measurements. The morphology of the metal oxide nanoparticles was investigated by TEM and surface compositions were analysed by XPS studies. Besides, the catalytic activity of these materials was tested in the combustion of methane at low concentration. The catalytic performance of these materials was compared to perovskite materials, usually considered as one of the most active mixed metal oxides for this reaction [21,22].

2. Experimental

2.1. Synthesis of host material SBA-15

The synthesis of SBA-15 material was carried out according to the procedure of Zhao et al. [18]. Firstly,

poly(ethylene oxide)–poly(propylene oxide)–poly-(ethylene oxide) (EO_{20}–PO_{70}–EO_{20}, Pluronic P123, BASF) tri-block copolymer was dispersed in an aqueous hydrochloric acid solution ($1 < pH < 2$) under vigorous stirring. After 1 h, a clear solution was obtained indicating a complete dissolution of the surfactant. Then, tetraethyl orthosilicate (TEOS) was added dropwise to the solution at 40 °C under stirring. Gelation and ageing were carried out at 40 °C for 24 h, followed by heating at 100 °C for 72 h in a sealed Teflon flask. The solid was filtered, washed several times with distilled water and dried at room temperature. Finally, the tri-block copolymer template was removed by calcination in air at 500 °C (heating rate 2 °C/min) for 6 h.

2.2. Preparation of supported metal oxides

The manganese and cobalt oxide supported catalysts on SBA-15 (Mn_3O_4/SBA-15 and Co_3O_4/SBA-15) were prepared according to the ''two-solvent'' technique [19]. SBA-15 was first suspended in dry hexane, used as hydrophobic solvent. Then, a desired amount of metal nitrate (7 or 30 wt.%) was dissolved in distilled water, the quantity corresponding to the pore volume of SBA-15 determined by N_2 sorption. This aqueous solution containing metal precursors was then added dropwise. The gel was allowed to age for 2 h under vigorous stirring. The solid was recovered by filtration and dried in air. The samples were finally calcined at 700 °C for 6 h (heating rate 2 °C/min) to obtain the desired metal oxides Co_3O_4 and Mn_3O_4 supported on SBA-15. Moreover, for comparison, Co_3O_4 metal oxide was also impregnated on silica gel (Grace, US) using the same technique.

2.3. Preparation of perovskite

$LaCoO_3$ perovskite was prepared according to the resin method from metallo-organic propionate precursors [23,24]. Firstly, lanthanum and cobalt acetate salts were dissolved in boiling propionic acid. Afterwards, the two solutions were mixed and stirred for 1 h under reflux conditions. Propionic acid was then evaporated until resin formation which hardened upon cooling. This resin was calcined at 700 °C for 4 h (heating rate 3 °C/min) to obtain the desired perovskite crystalline phase.

2.4. Characterisation techniques

The low-angle powder X-ray diffraction measurements were carried out on an X'PERT MDP apparatus (Philips, Cu Kα radiation) in the theta–theta geometry and associated to thin film optics, including programmable divergence slit (1/32°), parallel plate collimator, flat Ge monochromator and proportional Xe detector. The system was equipped with the TK450 camera of Anton Paar, as sample holder.

The wide-angle X-ray diffraction patterns were recorded on a Brucker D8 Advance diffractometer, with a Ni detector side filtered Cu Kα radiation (1.5406 Å) over a 2θ range of 5–90° and a position sensitive detector using a step size of 0.016° and a step time of 7 s. The diffraction spectra have been indexed by comparison with the JCPDS files (Joint Committee on Powder Diffraction Standards).

Nitrogen adsorption–desorption isotherms were measured on a Micromeritics ASAP using nitrogen as gas probe at −196 °C. Before measurement, the sample was evacuated under vacuum at 300 °C overnight to desorb moisture from the surface. The pore size distribution was determined from the adsorption branch of the isotherm and the SSA values were calculated using the BET model.

Transmission electron microscopy (TEM) measurements were performed on TOPCOM EM 002B microscope for high magnification and Hitashi S4800 FEG microscope equipped with SE, YAG-BSE and TE detectors. The samples were dispersed in chloroform and deposited on a carbon film supported on a Cu grid. EDX spectra were acquired using 20 kV primary electron energy to determine the average amount of metal oxides contained in the materials. Quantification was done using the standard-less ZAF correction method in the Genesis software from EDAX.

The XPS spectra were obtained using a Multilab 2000 XPS machine (Thermo). The pressure inside the chamber is 5.10^{-9} mbar during the analysis and the incident beam is Al Kα radiation ($h\nu = 1486.6$ eV). The spectra have been calibrated relative to the C $1s_{1/2}$ binding energy of contamination carbon, which was fixed at 285 eV.

2.5. Catalytic tests

The catalytic combustion of methane was performed under air in a fixed-bed reactor at atmospheric pressure. The quartz reactor is a U-shaped tube of 5 mm of inner diameter. The catalyst (150 mg) was packed between quartz wool plugs and placed in the middle part of the reactor. The void part of the reactor was filled by inert quartz pellets. The total gas flow of methane and air was set to 3 l/h, regulated by means of mass flow controllers (MFC, Brooks 5850 TR series).

The concentration of methane was set to 5% of its LEL (Lower Explosive Limit), *i.e.* 2500 ppm. The composition of the gas flow at the reactor outlet was analysed on-line by means of a Micro-GC 3000 gas analyzer (Agilent Technologies). A TCD detector was used for the Quad 200 which is composed by three modules with Porapack U (PPU), methylpolysiloxane (OV1) and molecular sieve 5 Å (MS5A) columns.

3. Results and discussion

3.1. Characterisation of supported metal oxides

The structures of synthesized Co_3O_4 and Mn_3O_4 in SBA-15 mesopores, 7% in weight, have been firstly examined by powder XRD, and the profiles are depicted in Figs. 1 and 2. Fig. 1 presents the low-angle diffraction patterns of bare SBA-15, Mn_3O_4/SBA-15 (7 wt.%) and Co_3O_4/SBA-15 (7 wt.%) samples. Three well-resolved peaks are detected for bare SBA-15 (Fig. 1a). These reflexions can be indexed to the (1 0 0), (1 1 0) and (2 0 0) diffractions of the ordered *p6mm* hexagonal space group [18]. It is noteworthy that only the (1 0 0) reflexion is still observed for Mn_3O_4/SBA-15 (7 wt.%) and Co_3O_4/SBA-15 (7 wt.%) materials (Fig. 1b and c). The incorporation of nanoparticles of metal oxides contributes to a drastic intensity decrease for Mn_3O_4/SBA-15 (7 wt.%) and Co_3O_4/SBA-15 (7 wt.%) (1 0 0) diffraction peak (Fig. 1b and c). This phenomenon was already observed by several authors [25,26]. Fig. 2a confirms the formation of crystallised Co_3O_4 cobalt oxide (JCPDS 065-3103). The broad peak between $10° \leq 2\theta \leq 30°$ corresponds to the mesoporous silica. The size of the nanoparticles was calculated using the Debye–Scherrer formula from the Full Width at Half Maximum (FWHM) of the (4 0 0) diffraction. A size of

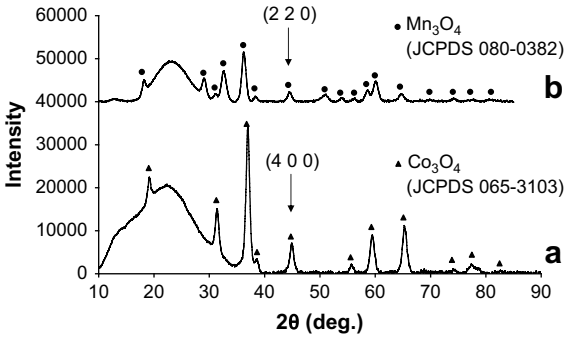

Fig. 2. Wide-angle XRD patterns of (a) Co_3O_4 and (b) Mn_3O_4 nanoparticles supported on SBA-15.

11 ± 2 nm was estimated for Co_3O_4 nanoparticles. According to Geus et al., the stable manganese oxide phases in air at 750 °C are either Mn_2O_3 or Mn_3O_4 [27]. The indexation of the different reflections shown by the wide-angle diffraction pattern (Fig. 2b) clearly evidenced the formation of Hausmannite Mn_3O_4 crystalline phase (JCPDS 080-0382) exclusively [28]. The particle size was calculated to be 10 ± 2 nm from the FWHM of the (2 2 0) diffraction peak of Mn_3O_4.

Representative nitrogen adsorption–desorption isotherms and the corresponding pore size distribution of bare SBA-15 and Mn_3O_4/SBA-15 are displayed in Figs. 3 and 4. The isotherm of siliceous SBA-15 exhibits a type IV isotherm with H1 hysteresis following the IUPAC classification [29] (Fig. 3a). This profile is a characteristic of mesoporous materials having one-dimensional cylindrical channels. A sharp inflection in the relative pressure (P/P_0) between 0.6 and 0.8 corresponds to capillary condensation within uniform mesopores and is a function of pore diameter. A narrow pore size distribution with a mean value of 68 Å is found for both the adsorption and desorption processes (Fig. 4a). The SSA and the pore volume of

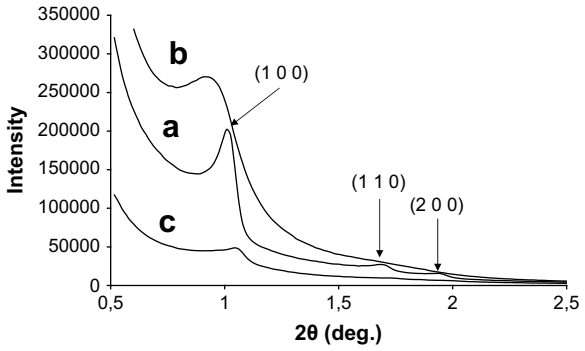

Fig. 1. Low-angle XRD patterns of (a) SBA-15, (b) Mn_3O_4/SBA-15 (7 wt.%) and (c) Co_3O_4/SBA-15 (7 wt.%).

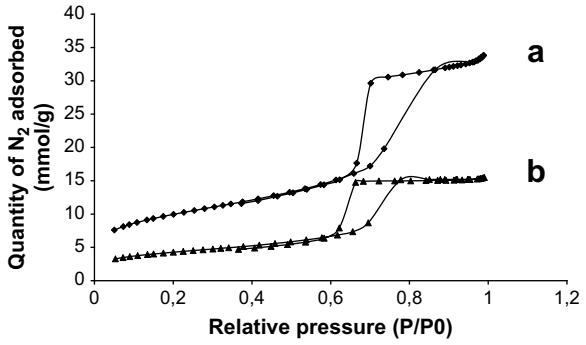

Fig. 3. Nitrogen adsorption–desorption isotherms of (a) bare SBA-15 and (b) Mn_3O_4/SBA-15 (7 wt.%).

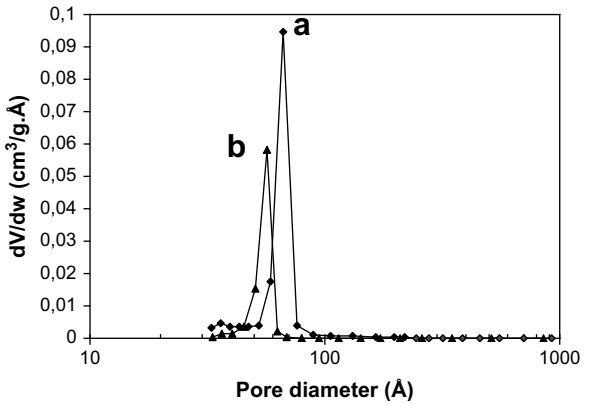

Fig. 4. Pore size distribution of (a) bare SBA-15 and (b) Mn_3O_4/SBA-15 (7 wt.%).

pristine SBA-15 are equal to 785 m^2/g and 1.17 ml/g, respectively. Besides, the isotherm of the Mn_3O_4/SBA-15 (7 wt.%) sample presents the characteristic sharp inflection in the same relative pressure compared to the bare SBA-15, but the quantity of adsorbed N_2 is lower (Fig. 3b). Vradman et al. reported a similar behavior for titanium oxide loaded on SBA-15 with the same concentration (7 wt.%) [30]. As concluded by those authors, the fact that the capillary condensation region becomes lower than the pristine SBA-15 reflects the filling of SBA-15 channels by metal oxides. This phenomenon is responsible for lower adsorption capacity of supported metal oxide samples and consequently reduced its SSA, pore volume and pore diameter. Indeed, the SSA and the pore volume of Mn_3O_4/SBA-15 (7 wt.%) are equal to 338 m^2/g and 0.53 ml/g, respectively. The pore size distribution for Mn_3O_4/SBA-15 (7 wt.%) sample is centered at a slightly lower pore diameter (56 Å) with respect to pristine SBA-15 (68 Å) (Fig. 4b). Vradman et al. also reported the same shift in pore size distribution between the titanium oxide impregnated on SBA-15 and bare SBA-15 [30,31]. It is important to note that the mesoporous structure was preserved after the catalytic runs. Similar results were obtained for Co_3O_4/SBA-15 (7 wt.%) sample: SSA = 316 m^2/g and pore diameter = 49 Å.

High-magnification TEM image (Fig. 5a) evidenced the presence of hexagonal arrangement of the porous network after Co_3O_4 impregnation. Mn_3O_4/SBA-15 microstructure was further investigated by TEM (Fig. 5b and c). Obviously, SBA-15 with a lower quantity of manganese oxide (7 wt.%) shows a homogeneous and high dispersion of nanoparticles formed exclusively within mesoporous channels (Fig. 5b). In contrast, SBA-15 having a higher manganese oxide

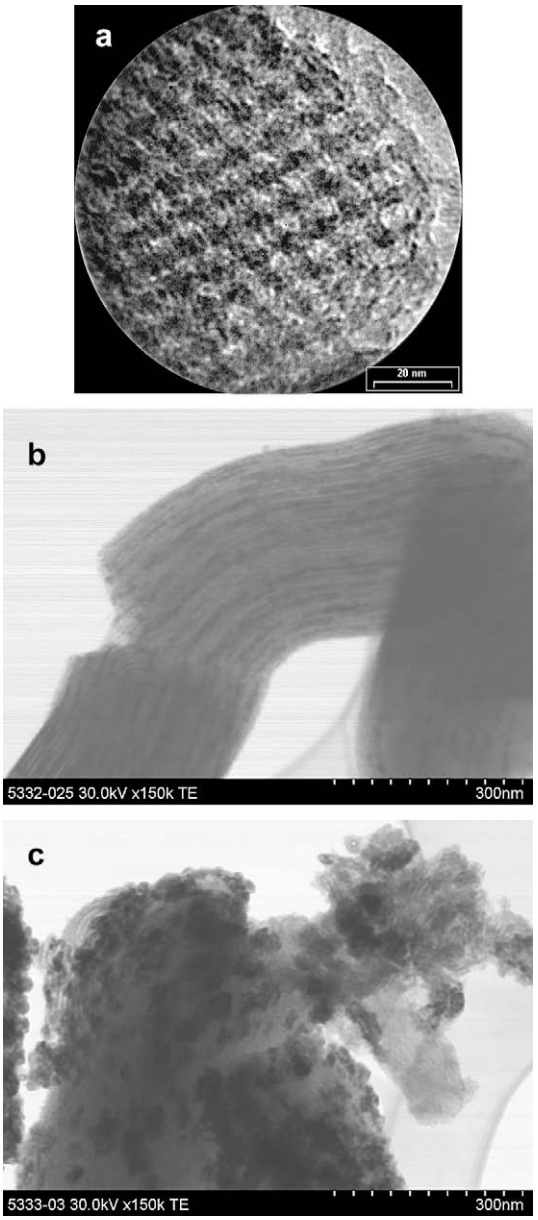

Fig. 5. TEM images of (a) Co_3O_4/SBA-15 (7 wt.%), (b) Mn_3O_4/SBA-15 (7 wt.%) and (c) Mn_3O_4/SBA-15 (30 wt.%).

loading (30 wt.%) presents larger aggregates (Fig. 5c). Despite uncertainties in the particle size, observed by TEM, due to changes in electron density [20], sizes of metal oxide nanoparticles (Mn_3O_4 and Co_3O_4) are consistent with the values calculated with Debye–Scherrer formula, *i.e.* 11 and 10 nm ± 2 nm for Co_3O_4 and Mn_3O_4, respectively.

EDAX analysis confirmed the presence of Co and Mn elements in the SBA-15 at the desired loadings. An average content of metal of 6.7 and 7.2 wt.% was

determined for Co_3O_4/SBA-15 (7 wt.%) and Mn_3O_4/SBA-15 (7 wt.%), respectively. Again, the efficiency of this two-solvent method is confirmed by the impregnation of nanoparticles having both controlled size and loading.

The results concerning the surface characterisation of the catalysts, performed by XPS analysis, are presented in Fig. 6 and Table 1. Fig. 6 illustrates the Si 2 p, O 1s and Mn 2p XPS spectra of the bare SBA-15 and Mn_3O_4/SBA-15 (7 and 30 wt.%) samples. The spectra of the different samples are very similar, and the variations in the binding energy (BE) values with

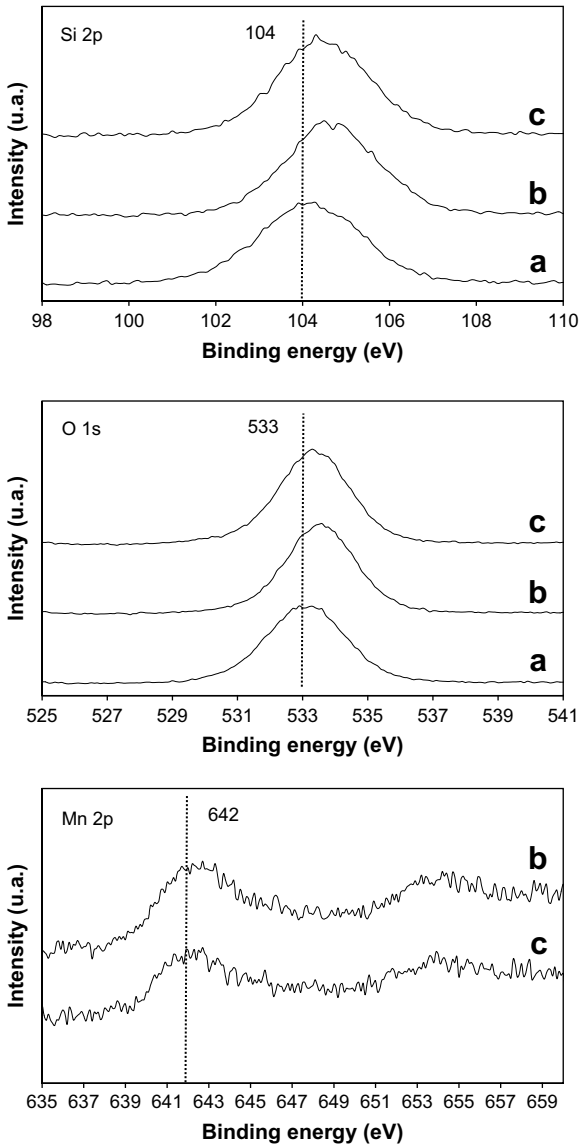

Fig. 6. Si 2p, O 1s and Mn 2p XPS spectra of (a) bare SBA-15, (b) Mn_3O_4/SBA-15 (7 wt.%) and (c) Mn_3O_4/SBA-15 (30 wt.%).

Mn_3O_4 loading are very small. Indeed, for all samples, symmetric Si 2p peaks are observed (Fig. 6). The small shift in the Si 2p binding energy of supported Mn_3O_4 samples compared to bare SBA-15 is due to the modification of the local environment of silicon in SBA-15 (Table 1). Furthermore, the O 1s signal shifts from BE = 533.5 eV for Mn_3O_4/SBA-15 (7 wt.%) to BE = 533.3 eV for Mn_3O_4/SBA-15 (30 wt.%). A shift from BE = 641.9 eV to BE = 641.5 in Mn $2p_{3/2}$ binding energy was also detected for the supported Mn_3O_4 samples. The shift of O 1s and Mn $2p_{3/2}$ peak positions towards lower binding energy, with the manganese oxide loading, indicates the possible modification of the oxidation state of the manganese oxide at the surface. According to the fact that stable manganese oxide phases in air at 750 °C are either Mn_2O_3 or Mn_3O_4 [27], we can suggest that a low manganese oxide loading (7 wt.%) can induce the presence of Mn_2O_3 species at the surface, whereas at higher manganese oxide loading (30 wt.%), Mn_3O_4 oxides become the only species present at the surface. The data in the literature confirm that the reduction of the Mn in the case of manganese oxide causes a decrease in both O 1s and Mn 2p binding energies [32,33]. Besides, the atomic content in percent (% At.) of Mn in Mn_3O_4/SBA-15 (7 wt.%) catalyst obtained by XPS is similar to the calculated one: 0.6% (Table 1). However, in the case of Mn_3O_4/SBA-15 (30 wt.%) the atomic content of Mn obtained by XPS: 0.8% is very low compared to the calculated one: 2.55%. This difference can mean that only a part of manganese oxide is accessible to the gas phase. This hypothesis is in line with the TEM images which confirm large aggregates in the case of high manganese oxide loading (30 wt.%).

3.2. Catalytic activity in methane combustion at low concentration

The catalytic activity of the different materials was tested in methane combustion. The resulting light-off curves show the CH_4 conversion according to the reaction temperature for 7 wt.% and 30 wt.% supported manganese oxides, 7 wt.% supported cobalt oxide and $LaCO_3$ perovskite. In order to compare the activity of the catalysts, the temperatures of 50% (T_{50}) and 90% (T_{90}) methane conversion were reported in Table 2. As shown in Fig. 7, the methane conversion as a function of temperature for Mn_3O_4/SBA-15 (7 and 30 wt.%) indicates that 7 wt.% supported manganese oxide was more active than the sample at 30 wt.%. Some differences of 18 °C and 27 °C in T_{50} and T_{90}

Table 1
Data of XPS studies.

	Si 2p		O 1s		Mn 2p		
	BE (eV)	% At.	BE (eV)	% At.	BE (eV)		% At.
SBA-15	104.1	35.8	533.1	64.2	–	–	–
Mn_3O_4/SBA-15 (7 wt.%)	104.5	33.8	533.5	65.6	641.9	653.7	0.6
Mn_3O_4/SBA-15 (30 wt.%)	104.3	32.4	533.3	66.8	641.5	653.1	0.8

temperatures are observed, respectively (Table 1). On the one hand, this better activity can be explained by the homogeneous dispersion of nanoparticles within the mesoporous silica channels, confirmed by TEM images (Fig. 5b and c). When the manganese oxide loading becomes important (30 wt.%), large aggregates are formed and consequently the catalytic activity decreases. On the other hand, the XPS studies clearly demonstrate that it is not necessary to impregnate on SBA-15 a large quantity of manganese oxide since only a fraction of the active phase is accessible to the gas phase. Besides, it is noteworthy that Co_3O_4/SBA-15 (7 wt.%) has the highest catalytic activity in methane combustion compared to Mn_3O_4/SBA-15 (7 and 30 wt.%). These results are in line with those generally reported for total oxidation of hydrocarbons: $Co_3O_4 > Mn_3O_4 > Cr_2O_3 > CuO$ [34–37]. It is interesting to note that the differences in the T_{50} between Co_3O_4/SBA-15 and Mn_3O_4/SBA-15 are less pronounced at T_{90}, *i.e.* at high temperatures (>570 °C). We can therefore suggest that the temperature of reaction strongly influences the behavior of the two catalysts.

At temperatures below 550 °C, Co_3O_4/SBA-15 exhibits the highest methane conversion. Whereas at temperature above 550 °C, a rapid increase in activity of Mn_3O_4/SBA-15 catalyst was observed, thus leading to a narrowing in the difference in methane conversion efficiency among Co_3O_4/SBA-15 and Mn_3O_4/SBA-15 catalysts. Such a change in metal oxide behavior with respect to the temperature was already pointed out by several authors, and can be explained by a change in methane total oxidation mechanism [38–40]. Prior, the materials must provide a high rate of molecular oxygen activation [38] to be considered as efficient catalysts in methane combustion. Hence, a large number of active sites which can coordinate oxygen molecules have to be present on the surface, to easily donate and accept electrons. These conditions are fully filled by metal oxides with an unfilled d-shell. Moreover, the catalysts should also allow a slow transformation of active oxygen into lattice oxygen [34]. At low temperature, the decomposition of oxidized surface species is generally the rate-determining step of total oxidation reaction. The oxygen mobility, in other words, the strength of metal–oxygen bonds is an important property for the activity of metal oxides in the deep oxidation process [38,40]. More the M–O bond is strong less the oxide is efficient because of the lack of O-lability [34]. Oxidation catalysts can also be classified as a function of the stability of the oxide. The enthalpy of metal–oxygen bond formation (ΔH°_{298}) is 105 kJ/mol lower for cobalt than for manganese. As a consequence, cobalt forms less stable oxides than manganese [39]. Consequently, Co_3O_4/SBA-15 is more efficient than Mn_3O_4/SBA-15 at temperatures below 550 °C, because of its high O-lability. Nevertheless, at temperatures higher than 550 °C, there is a change in

Table 2
T_{50} and T_{90} temperatures for the different catalysts.

	T_{50} temperature (°C)	T_{90} temperature (°C)
Co_3O_4/SBA-15 (7 wt.%)	506	576
Mn_3O_4/SBA-15 (7 wt.%)	534	588
Mn_3O_4/SBA-15 (30 wt.%)	552	615
$LaCoO_3$	514	591
Co_3O_4/SiO_2 (7 wt.%)	545	605

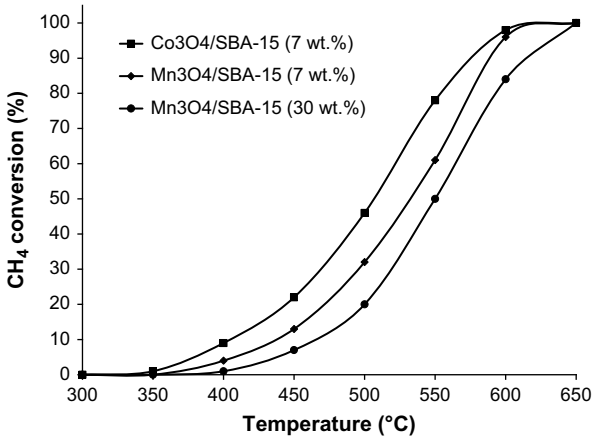

Fig. 7. Methane conversion as a function of temperature for manganese and cobalt oxides supported on SBA-15.

methane complete oxidation mechanism. The reaction rate becomes limited by the interaction between the oxidized reactant and the catalytic material, and is influenced positively by the strength of M–O bond. This tends to lead to the narrowing of the light-off curves of the two catalysts.

Because of their high thermal stability and an important oxygen mobility, mixed metal oxides such as perovskites (ABO_3) are particularly efficient catalysts in the oxidation of methane [11,41]. Arai and co-workers reported the high catalytic activities of $LaBO_3$ (B = Co or Mn) in the conversion of methane into carbon dioxide and water [9]. It was thus interesting to test $LaCoO_3$ perovskite in methane oxidation under the same conditions described previously, *i.e.* 150 mg of catalyst with the same catalyst bed length ($LaCoO_3$ diluted in SiO_2). Fig. 8 shows the light-off curves of this $LaCoO_3$ perovskite compared with supported metal oxides on SBA-15 (7 wt.%). It appears that the catalytic activity of Co_3O_4/SBA-15 (7 wt.%) and $LaCoO_3$ is similar. Besides, the conversion of methane over cobalt oxide Co_3O_4 (7 wt.%) loaded on silica gel support (SSA = 300 m^2/g) is also presented in Fig. 8. The Co_3O_4/SBA-15 (7 wt.%) catalyst has the highest activity in methane combustion compared to Co_3O_4/SiO_2 (7 wt.%). The efficiency of Co_3O_4/SBA-15 (7 wt.%) catalyst can be explained by a homogeneous dispersion of metal oxide nanoparticles within the channels of the mesoporous SBA-15. Therefore, it provides a confined active site, able to adsorb and activate methane efficiently on different crystallite faces. The preservation of the hysteresis loop and the SSA values for Co_3O_4/SBA-15 (7 wt.%) and Mn_3O_4/SBA-15 (7 wt.%) confirmed that the mesoporous structure is maintained after the catalytic run (not presented here).

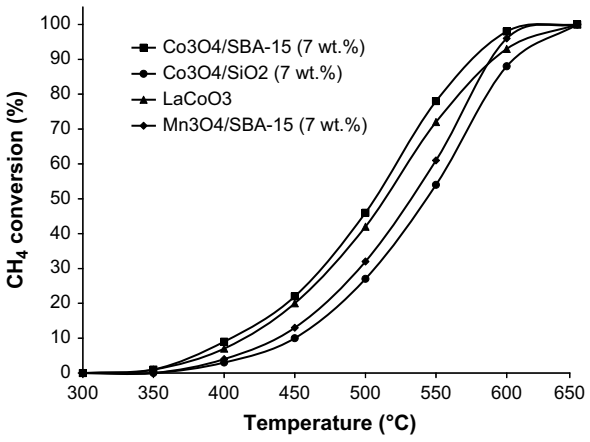

Fig. 8. Comparison between supported metal oxides on SBA-15 and $LaCoO_3$ perovskite. Influence of the nature of the silica support on methane catalytic combustion.

4. Conclusions

To conclude, a high dispersion of cobalt and manganese oxide nanoparticles was achieved within SBA-15 silica channels. This impregnation was carried out using a two-solvent preparation method, which allows a proper control of both the particle size and the loading of the metal oxides. An exhaustive characterisation of the mesoporous materials by XRD, BET, TEM and XPS was realized in order to correlate their structures with their catalytic activities. Indeed, some information obtained by TEM images and XPS studies were useful to understand the catalytic performance of the manganese oxides at different loading (7 wt.% and 30 wt.%) in methane combustion.

Co_3O_4/SBA-15 (7 wt.%) exhibited the highest catalytic performance in the conversion of methane to carbon dioxide and water even at 5% of LEL concentration. This opens up a novel route to produce efficient combustion catalysts, at low loading and without noble metals use.

The influence of the Co_3O_4 support in methane oxidation was investigated and confirmed the efficiency of the SBA-15 compared to silica gel. Thanks to its mesoporous structure, SBA-15 seems to present the appropriate pore architecture and size to ensure a high and homogeneous dispersion of Co_3O_4 and Mn_3O_4 oxides, thus creating a confinement media, being resistant to sintering.

Acknowledgements

The authors would like to thank GE Energy Products – Europe for financial support (GL). Dr. B. Heinrich (GMO-IPCMS, France), S. Libs, I. Zimmermann and C. Hulot are gratefully acknowledged for technical assistance. Finally, the authors would like to thank Dr J.-P. Tessonnier and G. Weinberg (Fritz-Haber-Institut, Berlin) for the TEM images.

References

[1] P. Gelin, M. Primet, Appl. Catal. B 39 (2002) 1.
[2] M. Moliere, P. Cozzarin, S. Bouchet, P. Rech, in: ASME Turbo Expo 2005, 6–9 June 2005, Reno.
[3] M. Molière, P. Cozzarin, S. Bouchet, P. Rech, in: ASME Turbo Expo 2006, 8–11 May 2006, Barcelona, Spain.
[4] S.J. Gentry, T.A. Jones, Sens. Actuators 10 (1986) 141.
[5] C.-H. Han, D.-W. Hong, S.-D. Han, J. Gwak, K.C. Singh, Sens. Actuators B 125 (2007) 224.
[6] I. Lundstrom, Sens. Actuators B 35 (1996) 11.

[7] D. Ciuparu, M.R. Lyubovsky, E. Altman, L.D. Pfefferle, A. Datye, Catal. Rev.—Sci. Eng. 44 (2002) 593.
[8] Y. Ozawa, Y. Tochihara, N. Mori, I. Yuri, J. Sato, K. Kagawa, Catal. Today 83 (2003) 247.
[9] H. Arai, T. Yamada, K. Eguchi, T. Seiyama, Appl. Catal. 26 (1986) 265.
[10] J.C. McCarty, H. Wise, Catal. Today 8 (1990) 231.
[11] M.A. Pena, J.L.G. Fierro, Chem. Rev. 101 (2001) 1981.
[12] J.M. Sohn, M.R. Kim, S.I. Woo, Catal. Today 83 (2003) 289.
[13] A. Corma, D. Kumar, Stud. Surf. Sci. Catal. 117 (1998) 201.
[14] B. Louis, C. Subrahmanyam, L. Kiwi-Minsker, B. Viswanathan, P.A. Buffat, A. Renken, Catal. Commun. 3 (2002) 159.
[15] E. Rivera-Muñoz, D. Lardizabal, G. Alonso, A. Aguilar, M.H. Siadati, R.R. Chianelli, Catal. Lett. 85 (2003) 147.
[16] A. Taguchi, F. Schuth, Microporous Mesoporous Mater. 77 (2005) 1.
[17] L. Vradman, M.V. Landau, M. Herskowitz, V. Ezersky, M. Talianker, S. Nikitenko, Y. Koltypin, A. Gedanken, J. Catal. 213 (2003) 163.
[18] D. Zhao, J. Feng, Q. Huo, N. Melosh, G.H. Fredrickson, B.F. Chmelka, G.D. Stucky, Science 279 (1998) 548.
[19] M. Imperor-Clerc, D. Bazin, M.D. Appay, P. Beaunier, A. Davidson, Chem. Mater. 16 (2004) 1813.
[20] I. Lopes, N. ElHassan, H. Guerba, G. Wallez, A. Davidson, Chem. Mater. 18 (2006) 5826.
[21] M. Alifanti, J. Kirchnerova, B. Delmon, D. Klvana, Appl. Catal. A 262 (2004) 167.
[22] T.V. Choudhary, S. Banerjee, V.R. Choudhary, Appl. Catal. A 234 (2002) 1.
[23] J.L. Rehspringer, J.C. Bernier, Mater. Res. Soc. Symp. Proc. 72 (1986) 67.
[24] G. Sinquin, C. Petit, J.P. Hindermann, A. Kiennemann, Catal. Today 70 (2001) 183.
[25] Y.-F. Han, F. Chen, K. Ramesh, Z. Zhong, E. Widjaja, L. Chen, Appl. Catal. B 76 (2007) 227.
[26] B. Tian, X. Liu, H. Yang, S. Xie, C. Yu, B. Tu, D. Zhao, Adv. Mater. 15 (2003) 1370.
[27] E.R. Stobbe, B.A. de Boer, J.W. Geus, Catal. Today 47 (1999) 161.
[28] V. Escax, M. Imperor-Clerc, D. Bazin, A. Davidson, C.R. Chimie 8 (2005) 663.
[29] K.S.W. Sing, D.H. Everett, R.A.W. Haul, L. Mosenu, R.A. Pierotti, J. Rouquerol, T. Siemieniewska, Pure Appl. Chem. 57 (1985) 603.
[30] R. Zukerman, L. Vradman, L. Titelman, C. Weidenthaler, M.V. Landau, M. Herskowitz, Microporous Mesoporous Mater 116 (2008) 237.
[31] L. Vradman, L. Titelman, M. Herskowitz, Microporous Mesoporous Mater. 93 (2006) 313.
[32] National Institute of Standards and Technology (NIST) X-ray Photoelectron Spectroscopy Database, http://srdata.nist.gov/xps/.
[33] F. Kapteijn, A.D. Van Langeveld, J.A. Moulijn, A. Andreïni, A. Vuurman, A.M. Turek, J.-M. Jehng, I.E. Wachs, J. Catal. 150 (1994) 94.
[34] M. O'Connell, A.K. Norman, C.F. Huttermann, M.A. Morris, Catal. Today 47 (1999) 123.
[35] A. Torncrona, M. Skoglundh, P. Thormahlen, E. Fridell, E. Jobson, Appl. Catal. B 14 (1997) 131.
[36] Y.F. Yu Yao, J. Catal. 39 (1975) 104.
[37] M.F.M. Zwinkels, S.G. Järås, P.G. Menon, Catal. Rev.—Sci. Eng. 35 (1993) 319.
[38] V.D. Sokolovskii, Catal. Rev.—Sci. Eng. 32 (1990) 1.
[39] J.J. Spivey, Ind. Eng. Chem. Res. 26 (1987) 2165.
[40] I. Yuranov, L. Kiwi-Minsker, A. Renken, Appl. Catal. B 43 (2003) 217.
[41] L.G. Tejuca, J.L.G. Fierro, J.M.D. Tascon, Adv. Catal. 36 (1989) 237.